PCCP

Potential energy function for apatites

Sven Hauptmann,†[a] Hagen Dufner,‡[a] Jürgen Brickmann,[a] Stefan M. Kast*[a] and R. Stephen Berry[b]

[a] *Institut für Physikalische Chemie, Technische Universität Darmstadt, Petersenstraße 20, 64287 Darmstadt, Germany*
[b] *Department of Chemistry, The University of Chicago, 5735 South Ellis Avenue, Chicago, IL 60637, USA*

Received 22nd August 2002, Accepted 10th December 2002
First published as an Advance Article on the web 2nd January 2003

An empirical potential energy function for fluor- and for hydroxyapatite is formulated and parametrised. The parameter optimisation involves a hierarchy of reference data and techniques comprising of quantum-chemical calculations for Coulomb interactions and intramolecular contributions, as well as experimental data and molecular dynamics simulations for the remaining nonbonded parameters. For fluorapatite both a flexible and a rigid phosphate model are derived, while for hydroxyapatite only the rigid variant is determined. Simulations with the final models reproduce the experimental crystal parameters within less than 1% deviation for a wide range of temperatures between 73 and 1273 K. In the case of flexible fluorapatite the computed and the experimental infrared spectra at 300 K agree excellently.

1 Introduction

Apatites are the dominant inorganic components of bones and teeth in vertebrates. Enamel, the hardest part of a tooth, essentially consists of hydroxyapatite.[1] Caries formation implies the hydrolysis of hydroxyapatite,[2,3] a phenomenon that can be apparently decelerated by fluoride ions. Understanding the demineralisation on a microscopic level and, possibly, controlling remineralisation for repairing tooth damages is an area of active current research. Biomineralisation processes in general involve the subtle interplay of an organic framework formed by *in vivo* synthesis and extracellular mineralisation. This enormously complex situation can be simplified by experimentally studying simpler model systems, for instance fluorapatite–gelatine composites that can be grown *in vitro*, and that show a remarkable chemical and structural similarity to enamel.[4,5]

Simple model systems are in principle amenable to theoretical investigations. Using experimentally found control parameters for the growth of fluorapatite in a gelatine matrix, a dynamical model was constructed based on fractal geometry.[6] Detailed microscopic models for instance capable of predicting elementary nucleation steps need yet to be developed. As a first step toward this goal we present in this article an empirical potential energy function for solid monoclinic hydroxyapatite $Ca_{10}(PO_4)_6(OH)_2$ (space group $P2_1/b$) and hexagonal fluorapatite $Ca_{10}(PO_4)_6F_2$ (space group $P6_3/m$) to be used in molecular dynamics (MD) simulations. The common structural motif of both apatites consists of parallel pipes of calcium ion triangles that are twisted alternately by 60°. Fluoride ions are located in the triangle centers while hydroxyl ions are placed slightly above.[7,8]

The parametrisation of a force field for such dominantly ionic systems containing flexible molecular entities constitutes a major challenge, entailing a significant amount of quantum-chemical calculations as well as the use of experimental data. We first describe the model function and the strategy towards reliable parameters along with the results. The optimal model is finally validated by comparison with structural and spectroscopic data from experiments.

2 Optimisation of the apatite models

2.1 Outline

The model function used in this work consists of the sum of intramolecular and pairwise additive, nonbonded intermolecular terms, $U = U_{\text{intra}} + U_{\text{inter}}$, where

$$u_{ij,\text{inter}}(r_{ij}) = \frac{1}{4\pi\varepsilon_0}\frac{q_i q_j}{r_{ij}} + w(\rho_i + \rho_j) \times \exp\left[\frac{R_i + R_j - r_{ij}}{\rho_i + \rho_j}\right] - \frac{C_i C_j}{r_{ij}^6} \quad (1)$$

comprises of a Born–Mayer–Huggins[9] (BMH) term with ε_0 being the vacuum dielectric constant, r_{ij} is the distance between particles i and j, q_i are the site charges, ρ_i, R_i, C_i are the BMH parameters, $w = 1.1552\times10^{-19}$ J Å^{-1} is the standard force.[10] The main difference to a standard Lennard-Jones/Coulomb expression is the exponential term covering atomic repulsion that is better suited for simulations over a wide range of temperatures. For fluorapatite both a rigid and a flexible phosphate model are constructed. The geometry of the hydroxyl group is taken as rigid throughout. Rigid model distances are directly taken from the experimental crystal structures.[7,8,11] The intramolecular phosphate potential reads

$$U_{\text{intra}} = \sum_{\text{bonds}}\frac{k_r}{2}(r_{ij} - r_0)^2 + \sum_{\text{angles}}\frac{k_\theta}{2}(\theta_{ijk} - \theta_0)^2 + \sum_{\text{angles}}\frac{k_{\text{UB}}}{2}(r_{ik} - r_0)^2. \quad (2)$$

Here, $k_{r,\theta,\text{UB}}$ are the force constants, θ_{ijk} are the bend angles between sites i, j, and r_0/θ_0 are equilibrium displacements.

† Present address: Roche Diagnostics GmbH, Sandhofer Str. 116, 68298 Mannheim, FRG.
‡ Present address: Silicon Graphics GmbH, Greschbachstr. 3, 76229 Karlsruhe, FRG.

"UB" denotes Urey–Bradley terms, *i.e.* harmonic stretching potentials over sites i and k constituting a bend angle.

The parametrisation of force fields, particularly for complex condensed phase systems, still remains a challenging and difficult task, often guided more by intuition in subdividing the necessary steps than by straightforward recipes; for recent reviews, see refs. 12–14. In our case, an obvious strategy consists of three consecutive stages:

(a) fitting of the site charges as to represent the quantum-chemically computed electrostatic field within the 3D periodic crystal environment;

(b) derivation of intramolecular phosphate parameters from gas-phase quantum-chemical calculations, assuming independence of the environment;

(c) optimisation of the remaining nonbonded parameters with respect to minimal deviations between computed and experimental crystal structures *via* MD simulations.

2.2 Methods

Quantum-chemical calculations were performed with Gaussian 94[15] on the HF level of theory, for the charge derivation using the Los Alamos National Laboratory LANL1DZ basis set[16] comprising effective core potentials, and for the phosphate ion *in vacuo* using the 6-31G* basis set. Normal frequencies were scaled by 0.89 according to empirical findings with the present basis.[17] Due to the known good performance of the Hartree–Fock approximation for the derivation of partial charges no other quantum-chemical models like for instance density functional theory have been used.

MD simulations were carried out in the canonical[18] (NVT) and in the isothermal–isobaric (NpT) ensembles using the Berendsen manostat.[19] Rigid body constraints were applied when necessary.[20,21] During parametrisation runs a time step of 1 fs was used, for production simulations to validate the force field a larger step of 3 fs was found to be sufficient. Nonbonded interactions were truncated using a shifted-force potential[22,23] with a cutoff distance of 13 Å. This value has been optimised with the final set of site charges (see below) by minimising the difference between the truncated and the true Madelung forces to below 2%.[23] The simulation boxes contained $4 \times 4 \times 5$ units cells (3260 atoms) for fluorapatite[7] and $2 \times 4 \times 5$ unit cells (3520 atoms) for hydroxyapatite.[8]

2.3 Site charges

Partial charges in a crystalline environment derived from electronic structure theory are influenced by the 3D lattice periodicity. In this work, we applied the Madelung point charge embedded cluster-self consistent field (MPCEC-SCF) approximation[24] that has been successfully used to predict nuclear quadrupole interactions in chlorine-substituted methanes. By construction, this technique is ideally suited to optimise electrostatic potential-derived (PD) charges[25] for use in solid state MD simulations: Based on an idea by Sauer,[26] quantum-chemical calculations are applied to a small cluster representing a crystal fragment, embedded in an environment of a large number of point charges that, together with the cluster charges, are determined as to approximately represent the true Madelung potential anywhere in space. The charges on the cluster sites and on the grid points are iteratively modified corresponding to new quantum-chemical calculations for each set of grid charges until self-consistency is reached, as schematically shown in Fig. 1: We start with an isolated cluster and compute its wave function Ψ_C from which PD charges q_C are determined. The cluster potential V_C and the Madelung potential V_M (from Ewald summation[27] of hypothetical translations of the cluster) are computed at the embedding grid points. A set of embedding grid charges q_U is fitted with respect to V_M–V_C; a new quantum-chemical calculation is performed for the cluster in the grid charge environment. We obtain a wave function Ψ_{C+U} that, after some iterations, is an approximation to the full crystal wave function Ψ_M.

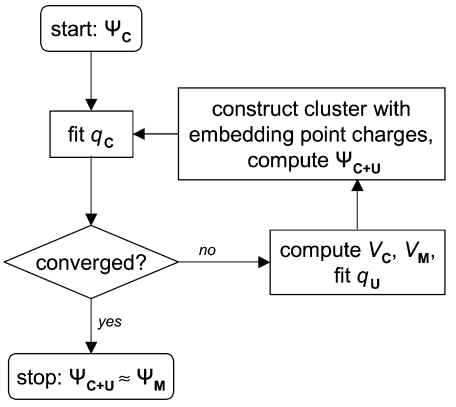

Fig. 1 Schematic flow chart of the Madelung point charge embedded cluster-self consistent field (MPCEC-SCF) method for the derivation of site charges within a crystal.

In our case typically one (fluorapatite) or two unit cells (hydroxyapatite) are taken as the basic cluster, surrounded by a grid corresponding to 50 times the number of cluster atoms. The cycles converge after around 10 iterations, the results are given in Table 1. Since there are only very small differences between fluor- and hydroxyapatite the charges for equivalent atom types were averaged. As a result, apatites appear to be remarkably ionic crystals, at least as far as the electric field within the phase is concerned. In contrast, Mulliken population analysis of full periodic density-functional calculations on fluorapatite done recently by Louis-Achille *et al.*[28] indicate a fair amount of covalent charge transfer between cation and anions. Since the final goal of using an empirical force field is the study of phase change and ion mobility, application of those population charges in solid state simulations would necessarily imply model expressions covering electronic polarisation and charge transfer.

2.4 Intramolecular parameters

Given a set of reference frequencies and the optimal geometry of the phosphate anion from quantum-chemical calculations, the intramolecular force field parameters were optimised using the dynamical simulated annealing approach described earlier.[12] Briefly summarised, the target function

$$S(\boldsymbol{\varphi}) = \sum_i p_i (O_i(\boldsymbol{\varphi}) - O_{i,\mathrm{ref}})^2, \qquad (3)$$

depending on a number of model parameters $\boldsymbol{\varphi} = \{\varphi_1, \varphi_2, \ldots\}$ and weights p_i, must be minimised with respect to deviations between model and reference observables, $O_i(\boldsymbol{\varphi})$ and $O_{i,\mathrm{ref}}$. The parameters are treated as dynamical variables moving in

Table 1 Partial atomic charges (in units of the elementary charge) of fluor- and hydroxyapatite; O(P) and O(H) denote the oxygen atoms in the phosphate and the hydroxide anions, respectively

Atom	Charge
Ca	+2.0
P	+2.6
O(P)	−1.4
O(H)	−1.6
H	+0.6
F	−1.0

a virtual potential defined by the target function according to

$$m_{\varphi,k}\ddot{\varphi}_k = -\frac{\partial}{\partial\varphi_k}S(\boldsymbol{\varphi}) + \tilde{\boldsymbol{R}} \tag{4}$$

where $m_{\varphi,k}$ are the virtual parameter masses, $\tilde{R}$ represents a stochastic heat bath force corresponding to a temperature T_φ in parameter space. T_φ is gradually decreased to zero allowing for a search of the global minimum. The virtual parameter masses $m_{\varphi,k}$ are adjusted during the annealing run in such a way that the local mass-weighted curvature of the target function is about the same for every parameter,[12] thus gaining maximum optimisation performance by balancing parameter sensitivity.

In this dynamical scheme the virtual forces acting on the parameters

$$\frac{\partial}{\partial\varphi_k}S(\boldsymbol{\varphi}) = 2\sum_i p_i(O_i(\boldsymbol{\varphi}) - O_{i,\mathrm{ref}})\frac{\partial O_i(\boldsymbol{\varphi})}{\partial\varphi_k} \tag{5}$$

need to be supplied with the parameter derivatives of the model observables. In the present case of an intramolecular force field we need the derivative of an eigenvalue λ_i of the mass-weighted Hessian $\boldsymbol{F}(\boldsymbol{q}_0,\boldsymbol{\varphi})$ at a given optimal geometry $\boldsymbol{q}_0$,[29]

$$\frac{\partial\lambda_i}{\partial\varphi_k} = \boldsymbol{\Lambda}_i^{\mathrm{T}}\frac{\partial\boldsymbol{F}(\boldsymbol{q}_0,\boldsymbol{\varphi})}{\partial\varphi_k}\boldsymbol{\Lambda}_i \tag{6}$$

where $\boldsymbol{\Lambda}_i$ denotes the corresponding eigenvector; for the derivative of an optimal geometry we have approximately[30]

$$\frac{\partial\boldsymbol{q}_0}{\partial\varphi_k} = -\boldsymbol{H}^{-1}(\boldsymbol{q}_0,\boldsymbol{\varphi})\frac{\partial\nabla U(\boldsymbol{q}_0,\boldsymbol{\varphi})}{\partial\varphi_k}. \tag{7}$$

In this case $\boldsymbol{H}$ is the true Hessian without mass-weighting.

After quantum-chemical geometry optimisation and normal mode calculations of a phosphate ion *in vacuo*, the annealing process was performed for intramolecular potential models with and without the Urey–Bradley term to check for the adequacy of a specified functional form. Structural data in the form of all interatomic distances and vibrational data were weighted equally; normal modes were assigned by maximising the overlap between model and reference eigenvectors. The results are given in Tables 2 and 3. The inclusion of a Urey–Bradley term for 1–3 intramolecular distance variations is apparently necessary, particularly for correctly representing the second mode. With the final set of parameters, the optimal distances are represented within 0.01 Å and the frequencies within 1 cm^{-1}.

2.5 Nonbonded parameters

The remaining nonbonded Born–Mayer–Huggins parameters were finally optimised with respect to minimising the difference between experimental and theoretical crystal structures at a nonzero temperature, necessitating MD simulations for the theoretical predictions. We again adopted the dynamical simulated annealing scheme that, in this case, can be quite naturally incorporated into the "real space" simulation protocol. If the observable is a thermal average to be computed from a simulation we obtain for instance in the isothermal–isobaric ensemble from

$$\langle O_i\rangle = Z^{-1}\int \mathrm{d}\boldsymbol{\Omega}O_i(\boldsymbol{\Omega})\exp[-\beta(H+pV)] \tag{8}$$

after some algebra[12]

$$\frac{\partial\langle O_i\rangle}{\partial\varphi_k} = -\beta\left(\left\langle O_i\frac{\partial U}{\partial\varphi_k}\right\rangle - \langle O_i\rangle\left\langle\frac{\partial U}{\partial\varphi_k}\right\rangle\right) \tag{9}$$

with $\beta = 1/k_{\mathrm{B}}T$, k_{B} being the Boltzmann constant and T the absolute temperature, H is the Hamiltonian, $\boldsymbol{\Omega}$ denotes all coordinates, momenta and the volume V at the pressure p, and Z is the partition function.

In contrast to earlier attempts to find suitable nonbonded parameters "on the fly" during a simulation, there is in this case neither need for monotonicity or global convexity of the target function,[31,32] nor are we restricted to find the next-nearest local minimum.[33] The procedure is schematically outlined in Fig. 2: n MD steps are performed in real space at each of which the simulation box is translated and rotated to match the experimental reference structure.[34] From these short runs under NpT conditions at 300 K and 1 bar, in our case 70 steps for each interval, the forces acting on the parameters $F_\varphi = -\partial S/\partial\varphi$ are computed according to eqns. (5) and (9), and a single step in parameter space is carried out. The experimental crystal parameters and atomic coordinates[7,8,11] act as reference observables. After 10 steps in parameter space new parameter masses are adjusted and the temperature T_φ is

Table 2 Normal frequencies/cm^{-1} of the phosphate anion: scaled quantum-chemical (QM) and force field calculations without (FF) and with Urey–Bradley (FF/UB) terms

Degeneracy	QM	FF	FF/UB
3	945.5	949.5	945.5
1	821.3	645.7	820.0
3	542.5	540.3	542.5
2	376.5	376.5	376.5

Table 3 Intramolecular force field parameters of the phosphate anion including Urey–Bradley (UB) terms: equilibrium displacements (r_0/Å and θ_0/degree) and force constants ($k_{r/\mathrm{UB}}$/kJ mol^{-1} $\mathrm{Å}^{-2}$ and k_θ/kJ mol^{-1} deg^{-2})

Type	r_0/θ_0	$k_{r/\mathrm{UB}}/k_\theta$
P–O stretch	1.27	2543.2
O–P–O bend	129.75	342.0
O–O UB	3.54	319.4

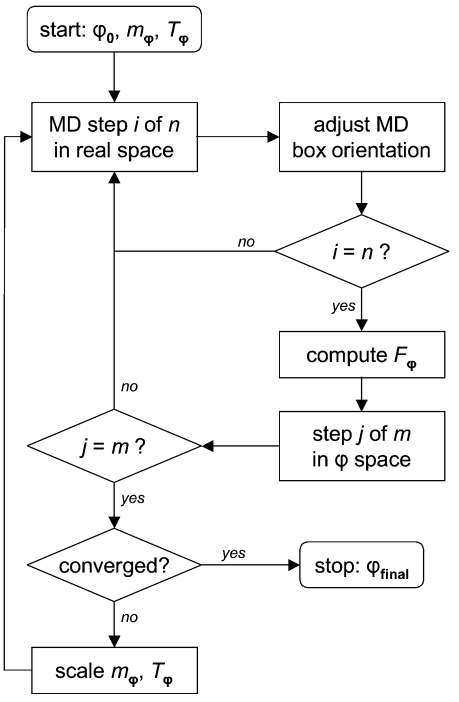

Fig. 2 Schematic flow chart for the "on the fly" determination of nonbonded potential parameters during an MD simulation.

slowly decreased. These steps are repeated until convergence is achieved. In contrast to the determination of the intramolecular parameters, in the intermolecular case the target function S appears to be very rugged, mainly because of the statistical uncertainties of the thermal averages. Therefore, the modified Huang *et al.*[35] cooling schedule

$$\beta_{\varphi,\mathrm{new}} = \beta_{\varphi,\mathrm{old}} + \lambda/\sigma_{\mathrm{old}} \tag{10}$$

was used with a small parameter $\lambda = 0.01$, $\beta_\varphi = 1/k_\mathrm{B}T_\varphi$ and σ being the standard deviation of the parameters' virtual total energy (as defined by the target function and the parameters' kinetic energy) during each annealing cycle. Cooling is faster in the early stages than close to final, very small parameter space temperatures; furthermore, increasing energy fluctuations lead to slower cooling.

The resulting parameters for the various models are listed in Tables 4 and 5. Due to the similarity of the results for the rigid models of both fluorapatite and hydroxyapatite the BMH parameters were averaged. The transferability of nonbonded parameters and charges emphasises the quality of the BMH functional form.

3 Final model validation

3.1 Crystal parameters

Solid state structural information from the final, optimised force field was tested against experimental crystal parameters[11] by performing 48 ps NpT simulations of fluorapatite and hydroxyapatite at a pressure of 1 bar and a number of different temperatures in a range between 73 and 1273 K. The results for the various models are summarized in Tables 6 and 7. Apparently the deviations are around 1% throughout, even less so for the rigid models. Preliminary simulations[36] employing the computationally more expensive Ewald summation[27] indicate very small changes around 1–2% as expected from the cutoff optimisation, in line with the deviation from experiment. Using shifted-force potentials as done in this work saves at least 20–30% computer time as compared even with the fastest particle-mesh Ewald implementations.[37]

3.2 Infrared spectra

As a measure for the quality of dynamical properties derived from the apatite force field we computed the infrared spectra of fluorapatite with the rigid and the flexible model, and compared them with experimental data. The spectra are derived from the cosine Fourier transform of the time correlation function of the total dipole moment[38]

$$c_{MM}(t) = \langle \boldsymbol{M}(0)\boldsymbol{M}(t)\rangle \tag{11}$$

with

$$\boldsymbol{M}(t) = \sum_i \boldsymbol{r}_i(t) q_i \tag{12}$$

where $\boldsymbol{r}_i$ is the position vector of particle i.

Expectation values were calculated from a 480 ps NVT simulation (coupling to the heat bath was checked not to influence the dynamics significantly) at 300 K. The resulting theoretical and experimental spectra are depicted in Fig. 3. The peaks at around 600 cm^{-1} and above as well as the complicated spectrum at very small wavenumbers where the experimental spectrum is not well resolved due to thermal noise can be attributed to the phosphate anion flexibility. Agreement of experiment and results from the flexible model is excellent. The main deviation is located around 600 cm^{-1} where the theory predicts a slight shift to larger wavenumbers as compared to experiment. Although beyond the scope of this work, the remaining discrepancy might be resolved by improving the intramolecular phosphate potential taking into account explicit anharmonicity and a larger fragment of the crystal for the vibrational analysis instead of a phosphate ion *in vacuo*.

Table 4 Nonbonded force field parameters for the systems with rigid phosphate. O(P) and O(H) denote the oxygen atoms in the phosphate and the hydroxide anions, respectively

Atom	ρ/Å	R/Å	$C/10^{-9}$ J$^{1/2}$ Å^3
Ca	0.080	1.30	1.2151
P	0.150	1.70	6.8351
O(P)	0.135	1.30	2.2784
O(H)	0.111	1.30	1.5189
H	0.010	0.10	0.0015
F	0.210	1.20	3.1897

Table 5 Nonbonded force field parameters for the flexible phosphate model of fluorapatite

Atom	ρ/Å	R/Å	$C/10^{-9}$ J$^{1/2}$ Å^3
Ca	0.079	1.30	1.3670
P	0.175	1.77	7.5946
O(P)	0.092	1.30	2.2784
F	0.209	1.21	3.1897

Table 6 Simulated and experimental[11] fluorapatite unit cell parameters for various temperatures, rigid and flexible models

T/K	Type	x/Å	y/Å	z/Å	α/degree	β/degree	γ/degree
73	Rigid	9.353	9.353	6.871	90.0	90.0	120.0
	Flex.	9.314	9.414	6.942	90.2	91.2	121.1
	Exp.	9.352	9.352	6.871	90.0	90.0	120.0
300	Rigid	9.355	9.355	6.901	90.0	90.0	120.0
	Flex.	9.347	9.440	6.960	90.3	90.9	120.9
	Exp.	9.370	9.370	6.883	90.0	90.0	120.0
600	Rigid	9.392	9.392	6.916	90.0	90.0	120.0
	Exp.	9.399	9.399	6.906	90.0	90.0	120.0
800	Flex.	9.431	9.430	6.993	90.0	90.0	120.0
	Exp.	9.417	9.417	6.922	90.0	90.0	120.0
1273	Rigid	9.460	9.460	6.964	90.0	90.0	120.0
	Flex.	9.526	9.527	6.989	90.0	90.0	120.0
	Exp.	9.460	9.460	6.964	90.0	90.0	120.0

Table 7 Simulated and experimental[11] hydroxyapatite unit cell parameters for various temperatures, rigid model

T/K	Type	x/Å	y/Å	z/Å	α/degree	β/degree	γ/degree
73	Simul.	9.433	18.852	6.900	90.0	90.0	120.0
	Exp.	9.377	18.754	6.881	90.0	90.0	120.0
300	Simul.	9.455	18.910	6.907	90.0	90.0	120.0
	Exp.	9.404	18.808	6.901	90.0	90.0	120.0
600	Simul.	9.488	18.976	6.916	90.0	90.0	120.0
	Exp.	9.441	18.882	6.928	90.0	90.0	120.0
1273	Simul.	9.556	19.111	6.940	90.0	90.0	120.0
	Exp.	9.523	19.046	6.987	90.0	90.0	120.0

4 Concluding remarks

The presented model potential function can be used immediately in studies of ion mobility in the solid state. For the important case of nucleation processes in the presence of gelatine mainly composed of collagen further modifications of the nonbonded parameters and the functional form are needed in

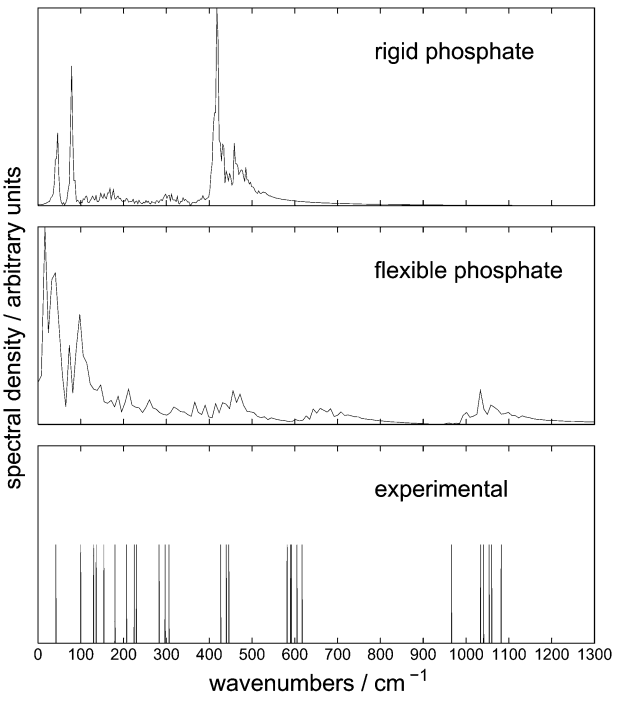

Fig. 3 Experimental and calculated infrared spectra of fluorapatite for the rigid (top) and flexible (middle) model at 300 K.

order to describe the interaction with the solvent and with the protein atoms. Since the optimised site charges in the solid state correspond basically to a fully ionic situation, this task can possibly be pursued without further quantum-chemical calculations simply by fitting a Lennard-Jones term to the repulsive and dispersion part of the BMH potential used here. The resulting parameters could then be combined with protein and water models in the usual way. With the recent progress in characterising the crystal structure of the collagen triple helix with high resolution[39] the goal to study theoretically elementary steps of biomineralisation processes on a microscopic level appears to be within reach.

Acknowledgements

S. M. K. wishes to thank the Alexander von Humboldt-Stiftung for financial support.

References

1 M. J. Bottero, J. Yvon and J. Vadot, *Eur. J. Mineral.*, 1992, **4**, 1347.
2 R. A. Young, W. van der Lugt and J. C. Elliott, *Nature*, 1969, **223**, 729.
3 M. Braun and C. Jana, *Chem. Phys. Lett.*, 1995, **245**, 19.
4 R. Kniep and S. Busch, *Angew. Chem.*, 1996, **35**, 2624.
5 S. Busch, U. Schwarz and R. Kniep, *Chem. Mater.*, 2001, **13**, 3260.
6 S. Busch, H. Dolhaine, A. DuChesne, S. Heinz, O. Hochrein, F. Laeri, O. Podebrad, U. Fietze, T. Weiland and R. Kniep, *Eur. J. Inorg. Chem.*, 1999, **10**, 1643.
7 K. Sundarsanan, P. E. Mackie and R. A. Young, *Mater. Res. Bull.*, 1972, **7**, 1331.
8 J. C. Elliot, P. E. Mackie and R. A. Young, *Science*, 1973, **180**, 1055.
9 F. G. Fumi and M. P. Tosi, *J. Phys. Chem. Solids*, 1964, **25**, 31; F. G. Fumi and M. P. Tosi, *J. Phys. Chem. Solids*, 1964, **25**, 45.
10 P. S. Yuen, R. M. Murfitt and R. L. Collin, *J. Chem. Phys.*, 1974, **61**, 2383.
11 D. Taylor, *Trans. Br. Ceram. Soc.*, 1988, **87**, 88.
12 S. M. Kast, J. Brickmann and R. S. Berry, in *Conceptual Perspectives in Quantum Chemistry*, ed. J.-L. Calais and E. Kryachko, Kluwer, NL, 1997, pp. 195–223.
13 P.-O. Norrby and T. Liljefors, *J. Comput. Chem.*, 1998, **19**, 1146.
14 J. Wang and P. Kollman, *J. Comput. Chem.*, 2001, **22**, 1219.
15 M. J. Frisch, G. W. Trucks, H. B. Schlegel, P. M. W. Gill, B. G. Johnson, M. A. Robb, J. R. Cheeseman, T. A. Keith, G. A. Petersson, J. A. Montgomery, K. Raghavachari, M. A. Al-Laham, V. G. Zakrewski, J. V. Oritz, J. B. Foresman, J. Cioslowski, B. B. Stefanov, A. Nanayakkara, M. Challacombe, C. Y. Peng, P. Y. Ayala, W. Chen, M. W. Wong, J. L. Andres, E. S. Replogle, R. Gomperts, R. L. Martin, D. J. Fox, J. S. Binkley, D. J. Defrees, J. Baker, J. P. Stewart, M. Head-Gordon, C. Gonzalez and J. A. Pople, *Gaussian 94*, Gaussian, Inc., Pittsburgh PA, 1995.
16 W. R. Wadt and P. J. Hay, *J. Chem. Phys.*, 1985, **82**, 284.
17 W. H. Hehre, L. Radon, P. v. R. Schleyer and J. A. Pople, *Ab Initio Molecular Orbital Theory*, Wiley, New York, 1986.
18 S. M. Kast and J. Brickmann, *J. Chem. Phys.*, 1996, **104**, 3732.
19 H. J. C. Berendsen, J. P. M. Postma, W. F. van Gunsteren, A. DiNola and J. R. Haak, *J. Chem. Phys.*, 1984, **81**, 3684.
20 J.-P. Ryckaert, G. Ciccotti and H. J. C. Berendsen, *J. Comput. Phys.*, 1977, **23**, 327.
21 G. Ciccotti, M. Ferrario and J.-P. Rykaert, *Mol. Phys.*, 1982, **55**, 549.
22 G. Schrimpf, M. Schlenkrich and J. Brickmann, *J. Phys. Chem.*, 1992, **96**, 7404.
23 H. Dufner, S. M. Kast, J. Brickmann and M. Schlenkrich, *J. Comput. Chem.*, 1997, **18**, 660.
24 G. Frantz, H. Dufner and P. C. Schmidt, *Z. Naturforsch.*, 1994, **49a**, 116.
25 C. M. Breneman and K. B. Wiberg, *J. Comput. Chem.*, 1990, **11**, 361.
26 J. Sauer, *Chem. Rev.*, 1989, **89**, 199.
27 P. P. Ewald, *Ann. Phys.*, 1921, **64**, 253.
28 V. Louis-Achille, L. de Windt and M. Defranceschi, *Int. J. Quantum Chem.*, 2000, **77**, 991.
29 F. S. Ganda-Kesuma and K. J. Miller, *J. Comput. Chem.*, 1994, **15**, 1291.
30 S. Lifson and A. Warshel, *J. Chem. Phys.*, 1968, **49**, 5516.
31 S. L. Njo, W. F. van Gunsteren and F. Müller-Plathe, *J. Chem. Phys.*, 1995, **102**, 6199.
32 C. D. Berweger, W. F. van Gunsteren and F. Müller-Plathe, *Chem. Phys. Lett.*, 1995, **232**, 429.
33 R. Faller, H. Schmitz, O. Biermann and F. Müller-Plathe, *J. Comput. Chem.*, 1999, **20**, 1009.
34 D. R. Ferro and J Hermans, *Acta Crystallogr., Sect. A*, 1977, **A33**, 345.
35 M. D. Huang, F. Romeo and A. L. Sangiovanni-Vincentelli, in *Proc. IEEE Int. Conference on Computer-Aided Design*, Santa Clara, 1986, pp. 381–384.
36 O. Hochrein, personal communication.
37 U. Essmann, L. Perera, M. L. Berkowitz, T. Darden, H. Lee and L. G. Pedersen, *J. Chem. Phys.*, 1995, **103**, 8577.
38 P. H. Berens and K. R. Wilson, *J. Chem. Phys.*, 1981, **74**, 4872.
39 R. Berisio, L. Vitagliano, L. Mazzarella and A. Zagari, *Protein Sci.*, 2002, **11**, 262.